RSC Advances

PAPER

View Article Online
View Journal | View Issue

Cite this: *RSC Adv.*, 2023, **13**, 20799

Boosted formic acid electro-oxidation on platinum nanoparticles and "mixed-valence" iron and nickel oxides†

Bilquis Ali Al-Qodami,[ab] Sayed Youssef Sayed,*[a] Hafsa H. Alalawy,[a] Islam M. Al-Akraa,[c] Nageh K. Allam [d] and Ahmad M. Mohammad *[a]

The modification of Pt nanoparticles (nano-Pt, assembled electrochemically onto a glassy carbon (GC) substrate) with hybrid multivalent nickel (nano-NiO_x) and iron (nano-FeO_x) oxide nanostructures was intended to steer the mechanism of the formic acid electro-oxidation (FAO) in the desirable dehydrogenation pathway. This binary modification with inexpensive oxides succeeded in mediating the reaction mechanism of FAO by boosting reaction kinetics "electron transfer" and amending the surface geometry of the catalyst against poisoning. The sequence of deposition was optimized where the a-FeO_x/NiO_x/Pt/GC catalyst (where "a" denotes a post-activation step for the catalyst at −0.5 V in 0.5 mol L^{-1} NaOH) reserved the best hierarchy. Morphologically, while nano-Pt appeared to be spherical (*ca.* 100 nm in average diameter), nano-NiO_x appeared as flowered nanoaggregates (*ca.* 56 nm in average diameter) and nano-FeO_x (after activation) retained a plate-like nanostructure (*ca.* 38 nm in average diameter and 167 nm in average length). This a-FeO_x/NiO_x/Pt/GC catalyst demonstrated a remarkable catalytic efficiency (125 mA mg_{Pt}^{-1}) for FAO that was *ca.* 12.5 times that of the pristine Pt/GC catalyst with up to five times improvement in the catalytic tolerance against poisoning and up to −214 mV shift in the FAO's onset potential. Evidences for equipping the a-FeO_x/NiO_x/Pt/GC catalyst with the least charge transfer resistance and the highest stability among the whole investigated catalysts are provided and discussed.

Received 19th May 2023
Accepted 23rd June 2023

DOI: 10.1039/d3ra03350c

rsc.li/rsc-advances

1. Introduction

The quest for clean, long-lasting, and efficient energy conversion devices, such as proton exchange membrane fuel cells (PEMFCs), to address the concerns of rising energy consumption and pollution has attracted great attention.[1,2] Due to the safety and storage issues associated with hydrogen, researchers have focused on developing PEMFCs, utilizing small organic molecules (*e.g.*, methanol, formic acid, and ethanol) as a fuel source.[3] Among these fuel cells (FCs), direct formic acid fuel cells (DFAFCs) use formic acid (FA, HCOOH) as a chemical energy source and operate with a high power density (~271 mW cm^{-2} at 30 °C (ref. 4) employing a Pd catalyst).[5–7] In fact, FA stands out among all other potential hydrogen carriers as a clean, nontoxic, nonflammable, stable, and renewable energy resource with a high energy density (2086 W h L^{-1}),[6,8] low fuel crossover rate through polymeric Nafion membranes, high theoretical electromotive force (open circuit voltage ~1.48 V), and low-cost for a liquid organic molecule under atmospheric conditions.[9–11] As such, FA is considered as an ideal power source for portable applications, vehicles, and small power generation devices.[12–14] In this regard, DFAFCs have received great interest in recent decades with the objective of developing a high-efficiency catalyst along with the illustration of the associated oxidation mechanism.[1,15] Thanks to the pioneer work of Capon and Parson, who used differential electrochemical mass spectrometry (DEMS) and provided evidence for a dual path mechanism for formic acid electro-oxidation (FAO);[16] direct dehydrogenation (desirable) to yield CO_2 and indirect dehydration (undesirable) to produce CO intermediate species that is because of its strong adsorption, the Pt surface became poisoned.[16–20] The Pt surface tends to mechanistically catalyze FAO *via* the cleavage of the C–O and C–H bonds mostly at low potentials, whereas the O–H bond is quickly cleaved at high potentials.[21] Among the most inspected platinum group metals, Pd-based electrocatalysts have exhibited better FAO activities through the preferential dehydrogenation pathway than those based on Pt. However, they also suffer from much lower

[a]*Chemistry Department, Faculty of Science, Cairo University, Cairo 12613, Egypt. E-mail: ammohammad@cu.edu.eg; sysayed@sci.cu.edu.eg*

[b]*Chemistry Department, Faculty of Education and Applied Science, Hajjah University, Yemen*

[c]*Department of Chemical Engineering, Faculty of Engineering, The British University in Egypt, Cairo 11837, Egypt*

[d]*Energy Materials Laboratory, School of Sciences and Engineering, The American University in Cairo, New Cairo 11835, Egypt*

† Electronic supplementary information (ESI) available. See DOI: https://doi.org/10.1039/d3ra03350c

stabilities in extreme acidic and oxidative environments, not to mention the toxic CO species produced by a reverse CO_2 reduction, which poisons the Pd surface.[22–24] Because of its partially filled 5d orbital, Pt has been deemed the best option for a single metal electrocatalyst for the cathodes and anodes of FCs to date.[25] To enhance the encountered kinetics of FAO and minimize the adsorption of CO on Pt, numerous strategies have been investigated with the focus on investigating the catalytic activity of Pt-based binary and ternary alloys/composites, including elements such as Pb, Bi, Rh, Au, Pd, and Sn.[11,26,27] Modulating the morphology of the Pt-based catalysts by alloying with other elements is considered an effective way to reduce the poisoning by CO and to increase the durability of the catalysts through a bifunctional mechanism and/or enhanced electronic, ensemble, and synergistic effects for the employed elements.[11,28,29] The modification of Pt with transition metal oxide nanostructures could improve Pt's selectivity for the dehydrogenation pathway of FAO. The fabrication of metal oxides that exhibit an inverse switch between low and high oxidation states at a potential close to the thermodynamic potential of a target reaction is the current point of interest.[30] Furthermore, metal oxides with different valence states (*e.g.*, FeO_x, MnO_x, and WO_x) contain significant oxygen vacancies, compared with metal oxides with a single valence state. Mixed-valence metal oxides have also been applied as reduced substrates for CO oxidation.[12] The current study is interested in investigating FAO at Pt nanoparticles (nano-Pt) that were deposited onto a glassy carbon (GC) substrate and amended with nickel (nano-NiO_x) and iron (nano-FeO_x) oxides nanostructures. The modification of nano-Pt with nano-NiO_x and/or nano-FeO_x was planned from their excellent catalytic characteristics toward the oxidation of small organic molecules.[6,31–33] Interestingly, with this modification, the catalyst's cost was reduced by lowering the Pt content, and the catalyst's activity toward FAO was boosted with a longer lifetime and a remarkable tolerance against CO poisoning, which are the requirements to enhance the performance of DFAFCs.

2. Experimental section

2.1. Materials and characterization methods

All the chemicals used were of the highest quality and used without further purification. Potassium hexachloroplatinate (K_2PtCl_6), ferrous sulfate heptahydrate ($FeSO_4 \cdot 7H_2O$), nickel sulfate hexahydrate ($NiSO_4 \cdot 6H_2O$), sodium hydroxide pellets (NaOH), sulfuric acid (H_2SO_4), sodium sulphate (Na_2SO_4), disodium hydrogen phosphate (Na_2HPO_4), hydrochloric acid (HCl), and formic acid (HCOOH) were purchased from Sigma Aldrich, Riedel-de Haen, and Merck. Electrochemical measurements and electrochemical impedance spectroscopy (EIS) were performed in a conventional three-electrode glass cell at room temperature (25 ± 1 °C) using an EG&G potentiostat (model 273A) operated with Echem 270 software. A glassy carbon (GC, 3.0 mm) disk was connected before and after modifications with the different catalytic ingredients as the working electrode, while Ag/AgCl/KCl (sat.) and Pt wire served as the reference and counter electrodes, respectively. The GC electrode was mechanically polished with Al_2O_3 slurries, followed by 10 min sonication in water and finally rinsed with distilled water. A field emission scanning electron microscope (FE-SEM, FEI, QUANTA FEG 250) connected with an energy dispersive X-ray spectrometer (EDX) unit was applied to identify the morphologies and elemental composition of the prepared catalysts. ImageJ software was used to calculate the average particle size distributions from the FE-SEM images for the prepared nanocatalysts. An X-ray powder diffractometer (PANalytical, Empyrean) operated with Cu target (λ = 1.54 Å) was used to investigate the crystallographic structure of the prepared catalysts.

2.2. Catalyst preparation

The deposition of nano-Pt on the GC electrode was carried out *via* potential step electrolysis (from 1 to 0.1 V) for 300 s in 0.1 mol L^{-1} H_2SO_4 containing 1 mmol L^{-1} K_2PtCl_6 solution. Electrode modification with nano-NiO_x was achieved in three sequential steps. Metallic nickel (Ni) nanostructures were deposited on the GC surfaces by applying a constant voltage of −1.0 V for 120 s in 1.0 mmol L^{-1} $NiSO_4 \cdot 6H_2O$ and 0.1 mol L^{-1} Na_2SO_4 solution. The metallic nickel nanostructures were then converted to nickel oxide (passivation step) by cycling the potential from −0.5 to 1 V at 200 mV s^{-1} in 0.1 mol L^{-1} phosphate buffer solution (PBS, pH = 7).[15] Finally, the as-prepared electrode was activated by cycling the potential between −1 and 0.6 V at a scan rate of 200 mV s^{-1} for 25 cycles in 0.5 mol L^{-1} NaOH solution.[26,30] The electrodeposition process of the nano-FeO_x was carried out in 0.02 mol L^{-1} $FeSO_4 \cdot 7H_2O$ aqueous solution by running a two-cycle potential scan between −0.855 and −1.205 V at a scan rate of 100 mV s^{-1},[33–35] followed by an activation step for the electrodeposited nano-FeO_x by holding the applied voltage at −0.5 V for 10 min in 0.2 mol L^{-1} NaOH solution.

3. Results and discussion

3.1. Electrochemical characterization

The electrochemical characterization of the catalyst can sometimes have the ability to track minute amounts of even minor electroactive species, which are presumably undetectable under typical material characterization techniques. The electrochemical measurements were performed to confirm the successful deposition of all components of the catalyst. Hence, Fig. 1 and 2 demonstrate the cyclic voltammograms (CVs) in alkaline (0.5 mol L^{-1} NaOH) and acidic (0.5 mol L^{-1} H_2SO_4) media, respectively, on the GC-modified electrodes. The CV of the nano-Pt/GC electrode (curve a in Fig. 1) depicts the typical characteristics of a polycrystalline Pt electrode in alkaline medium, including the characteristic surface oxidation (Pt/PtO) extending from *ca.* −0.2 to 0.6 V, surface reduction (PtO/Pt) at *ca.* −0.35 V, and the two peaks for the $H_{ads/des}$ appearing between −0.6 and −1.0 V.[36] At the nano-NiO_x/GC electrode (curve b, Fig. 1), the well-defined redox couple observed at *ca.* 0.4 V is assigned to the $Ni(OH)_2$/NiOOH reversible transformations, according to eqn (1).[22,26,30,37]

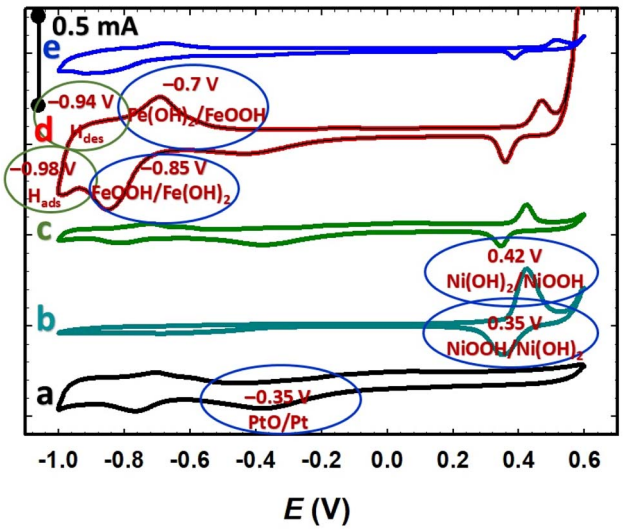

Fig. 1 CVs obtained for the Pt/GC (a), NiO_x/GC (b), NiO_x/Pt/GC (c), FeO_x/NiO_x/Pt/GC (d), and a-FeO_x/NiO_x/Pt/GC electrodes (e) in 0.5 mol L^{-1} NaOH solution at a scan rate of 200 mV s^{-1}.

$$Ni(OH)_2 \leftrightarrow NiOOH + H^+ + e^-,\ e^0_{rev} = 1.36\ V \quad (1)$$

Interestingly, in the case of the NiO_x/Pt/GC electrode (curve c, Fig. 1) for which nano-Pt was first deposited followed by nano-NiO_x, a remarkable decrease in the intensity of the PtO reduction and the characteristic $H_{ads/des}$ peaks was observed, indicating a significant decrease in the accessible surface area of Pt due to the deposition of the nano-NiO_x, which showed a phase transformation at *ca.* 0.4 V. At the FeO_x/NiO_x/Pt/GC electrode (curve d, Fig. 1) where the nano-FeO_x structures were finally deposited on the NiO_x/Pt/GC electrode, several new features appeared. This included the well-defined redox peak couple in alkaline medium at *ca.* −0.70 V (oxidation) and −0.85 V (reduction), which could likely be entrusted to the Fe^{2+}/Fe^{3+} transformations,[38–40] with the early and intense evolution of oxygen at the end of the CV scan in the positive direction of voltages, if compared to other aforementioned catalysts in Fig. 1. After the activation step for the FeO_x/NiO_x/Pt/GC electrode at −0.50 V and here, referred as the a-FeO_x/NiO_x/Pt/GC electrode (curve e, Fig. 1), the characteristic features of the Pt, NiO_x, and FeO_x nanoparticles were observed but with lower intensities compared to what was observed for the non-activated surface (curve d).

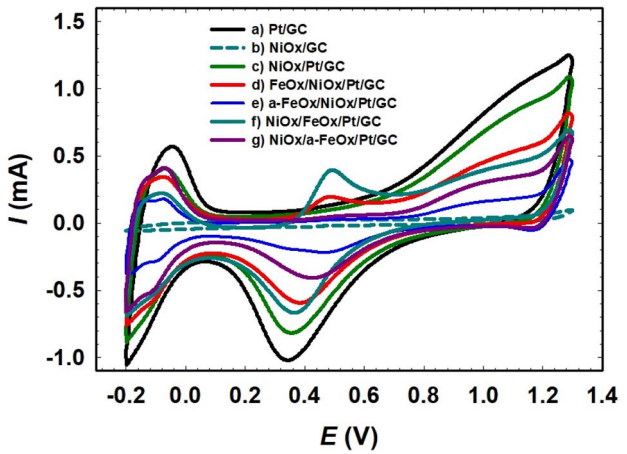

Fig. 2 CVs obtained for the Pt/GC (a), NiO_x/GC (b), NiO_x/Pt/GC (c), FeO_x/NiO_x/Pt/GC (d), a-FeO_x/NiO_x/Pt/GC (e), NiO_x/FeO_x/Pt/GC (f), and NiO_x/a-FeO_x/Pt/GC (g) in 0.5 mol L^{-1} H_2SO_4 at a scan rate of 200 mV s^{-1}.

Fig. 2 shows the CVs of the prepared catalysts in 0.5 mol L^{-1} H_2SO_4. For the Pt/GC electrode (curve a), an exemplary CV was observed, featuring the polycrystalline Pt surfaces in acidic media, with the characteristic Pt/PtO (*ca.* 0.34 V) and $H_{ads/des}$ (−0.2 to 0.1 V) transformation peaks. It is worth pointing out that these peaks (PtO → Pt or H_{des}) can be used to assess the electrochemically active surface area (ECSA) of Pt in the catalyst, which can be influenced by numerous factors such as the different mole ratios and structures of the catalysts' components. The deposition conditions of the catalytic components (nano-FeO_x and nano-NiO_x), including the electrolyte's composition and concentration, operating temperature, applied potential, and post-activation, can certainly justify not only the coverage of this component onto the Pt surface but also its facet orientation, which in turn affect the ECSA of the catalyst. However, in this investigation, we avoided calculating the ECSA from the PtO → Pt reduction peak as it might interfere with the reduction of nano-FeO_x. The steps for the ECSA calculation from the H_{des} peak in Fig. 2 are detailed in the ESI (see Fig. S1†). The ECSA (cm^2) was calculated employing the monolayer adsorption charge for platinum (210 μC cm^{-2}).[32,34,41] The calculated ECSA values of the studied catalysts were 0.200, 0.126, 0.110, 0.070, 0.110, and 0.090 cm^2 for Pt/GC, NiO_x/Pt/GC, FeO_x/NiO_x/Pt/GC, a-FeO_x/NiO_x/Pt/GC, NiO_x/FeO_x/Pt/GC, and NiO_x/a-FeO_x/Pt/GC, respectively, and the corresponding data are listed in Table 1.

The a-FeO_x/NiO_x/Pt/GC electrode had the lowest ECSA value when compared to Pt/GC catalyst. Interestingly, the electrodeposition of nano-FeO_x (*vide infra* for the observed morphology) on top of the NiO_x/Pt/GC electrode, and especially after activation at −0.5 V (curve e), resulted in a considerable decrease in the peak current intensities for the Pt/PtO oxidation and $H_{ads/des}$ transformations. The ECSA was utilized to estimate the surface coverage (θ) of the nano-NiO_x or/and nano-FeO_x on the Pt/GC electrodes according to $\left(\theta = \left(1 - \frac{A_{mod}}{A_{unmod}}\right) \times 100\right)$, where, A_{mod} and A_{unmod} refer to the ECSA of the modified and the unmodified Pt/GC electrodes, respectively. The surface coverages of nano-NiO_x or/and nano-FeO_x nanoparticles for the NiO_x/Pt/GC, FeO_x/NiO_x/Pt/GC, a-FeO_x/NiO_x/Pt/GC, NiO_x/FeO_x/Pt/GC, and NiO_x/a-FeO_x/Pt/GC modified electrodes were estimated to be *ca.* 37, 45, 65, 45, and 55%, respectively. It is worth noting here that the CV of the NiO_x/Pt/GC electrode in acidic medium did not display any redox peaks characteristic for nickel oxides, which are unstable and dissolve in acidic media,[42] whereas the redox peak for the Fe^{2+}/Fe^{3+} transformation appeared in the

Table 1 A summary of the important catalytic indices of Fig. 5A

Electrode	ECSA (cm^2)	I_p^d (mA cm^{-2})	I_p^{ind} (mA cm^{-2})	I_b (mA cm^{-2})	I_p^d/I_p^{ind}	I_p^d/I_b	E_{onset} (mV)
Pt/GC	0.200	1.2	0.6	6.5	2.0	0.18	42
NiO_x/Pt/GC	0.126	3.3	0.4	5.9	8.3	0.56	−102
FeO_x/NiO_x/Pt/GC	0.110	4.8	0.3	5.5	16.0	0.87	−178
a-FeO_x/NiO_x/Pt/GC	0.070	7.5	0.3	8.6	25.0	0.87	−172
NiO_x/FeO_x/Pt/GC	0.110	3.8	0.3	5.7	12.7	0.67	−102
NiO_x/a-FeO_x/Pt/GC	0.090	3.6	0.40	7.0	9.0	0.51	−32

potential range from 0.4 to 0.6 V, confirming the successful deposition of the iron species.

3.2. Morphological and surface characterization

The catalyst's structural and morphological information are not only imperative for the elucidation of the employed catalytic mechanisms but also for the design and further development of different electroactive materials.[43] As such, we characterized the morphology of the different studied electrodes, as shown in the FE-SEM micrographs in Fig. 3 (the particle size distributions are depicted whenever possible in the insets of Fig. 3) for the Pt/GC, NiO_x/GC, NiO_x/Pt/GC, FeO_x/NiO_x/Pt/GC, and a-FeO_x/NiO_x/Pt/GC electrodes. Interestingly, Pt was electrodeposited on the bare GC substrate in the form of spherical nanoparticles with an average particle diameter of *ca.* 100 nm (Fig. 3a). On the other hand, nano-NiO_x in the passivated NiO_x/GC surface was observed in the form of nanoparticles, with an average particle diameter of *ca.* 24.0 nm, along with aggregated dendritic structures at the micrometer scale (*ca.* 10 μm) (Fig. 3b). The deposition of nano-NiO_x in the NiO_x/Pt/GC-modified electrode (Fig. 3c), however, resulted in the appearance of spherical flower-like nanoaggregates (average particle diameter of *ca.* 56 nm) that uniformly covered a large portion of the GC. Further

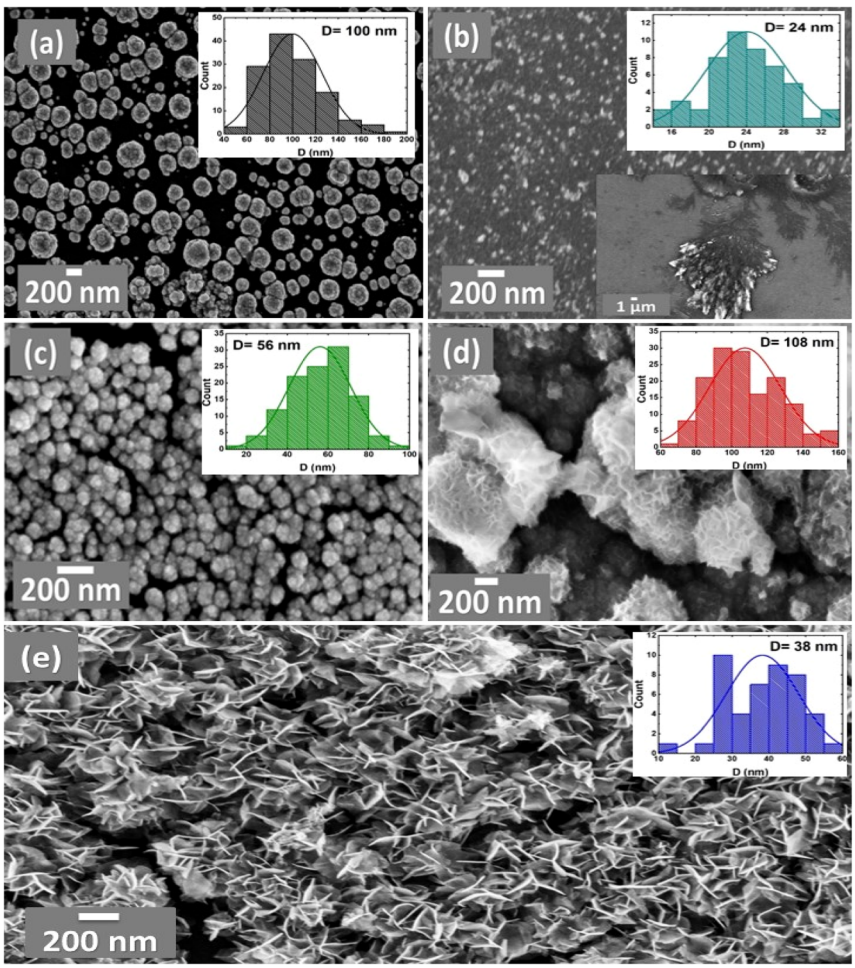

Fig. 3 FE-SEM images and particle size distributions (top right insets) obtained for the Pt/GC (a), NiO_x/GC (b), NiO_x/Pt/GC (c), FeO_x/NiO_x/Pt/GC (d), and a-FeO_x/NiO_x/Pt/GC (e) electrodes. Lower right inset of (b) is for the Ni/GC electrode before passivation.

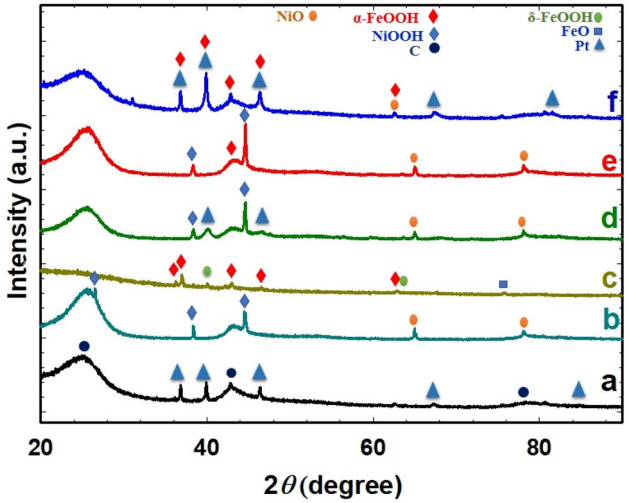

Fig. 4 XRD patterns for Pt/GC (a), NiO_x/GC (b), FeO_x/GC (c), NiO_x/Pt/GC (d), FeO_x/NiO_x/Pt/GC (e), and a-FeO_x/$NiO_x$$NiO_x$/Pt/GC (f) electrodes.

modification with nano-FeO_x resulted in the formation of nanoparticles aggregates with an average diameter of *ca.* 108 nm (Fig. 3d). The activation of the latter electrode at −0.5 V in 0.2 mol L^{-1} NaOH solution was found to completely change the morphology of the FeO_x/NiO_x/Pt/GC electrode and the appearance of plate-like nanostructures (*ca.* 38 nm average diameter and 167 nm average length, Fig. 3e). The elemental composition of the FeO_x/NiO_x/Pt/GC electrode was investigated by EDX (Fig. S2†), which indicated the existence of Pt, Ni, and Fe as well as a high percentage (51.67%, at%) of oxygen, thus revealing the oxide nature of the catalytic surface. The observed sulfur signal might be attributed to the surface adsorption of sulphate ions (SO_4^{2-}) that was not removed after copiously rinsing with water following the deposition step.

Fig. 4 shows the observed XRD patterns for the different studied electrodes and reveals the crystalline nature of nano-Pt, nano-NiO_x, and nano-FeO_x species. In all the XRD profiles shown in Fig. 4, diffraction peaks corresponding to the (0 0 2), (1 0 1), and (1 1 0) planes of the carbon substrate appeared at 2θ values of *ca.* 25.0, 43.3, and 78.0°, respectively (JCPDS Card No. 00-026-1077).[42,44] As shown in Fig. 4a, the five diffraction peaks at 2θ of 37.0, 39.8, 46.3, 67.5, and 81.3° corresponded to the Pt (1 0 1), Pt (1 1 1), Pt (2 0 0), Pt (2 2 0), and Pt (3 1 1) planes, respectively, for face centered cubic (fcc) Pt (JCPDS Card No. 00-004-0802).[32,45,46] For the NiO_x/GC electrode (Fig. 4b), diffraction peaks observed at *ca.* 2θ of 25.2, 37.9, and 43.1° were assigned to the NiOOH phase (JCPDS Card No. 00-006-0075), while the other two diffraction peaks observed at 2θ of 62.2 and 78.6° were assigned to the NiO phase (JCPDS Card No. 01-071-4750).[26,47] On the other hand, for the FeO_x/GC electrode (Fig. 4c), the diffraction peaks for the α-FeOOH phase were detected at 2θ of 36.2, 36.8, 42.1, 46.3, and 62.5° corresponding to the (0 4 0), (1 1 1), (1 4 0), (0 4 1), and (0 0 2) crystallographic planes, respectively (JCPDS Card No. 29-0713).[48–51] Moreover, the typical characteristic peaks for the δ-FeOOH phase were observed at *ca.* 2θ of 40.13 and 62.89° corresponding to the (1 0 1) and (1 1 0) planes, respectively.[52] In addition, a diffraction peak, corresponding to the (2 2 0) facet of iron(II) oxide (FeO), was observed at 2θ 75.6° (JCPDS Card No. 02-1186).[53] The same peaks of nano-Pt and nano-NiO_x with their previous assignments were obvious for the NiO_x/Pt/GC catalyst (Fig. 4d). It is also worth noting that the diffraction signal from the Pt structures was not revealed after the deposition of nano-FeO_x in the FeO_x/NiO_x/Pt/GC electrode (Fig. 4e), indicating an effective coating with nano-FeO_x atop the Pt facets, but the diffraction peaks corresponding to NiOOH, NiO, and α-FeOOH were observed. However, after the activation of the FeO_x/NiO_x/Pt/GC electrode at −0.5 V (Fig. 4f), the Pt diffraction peaks reappeared together with only the NiO and α-FeOOH diffractions. This indicates a partial detachment/dissolution of α-FeOOH covering the Pt structures while boosting the surface oxidation of Fe^{2+} to Fe^{3+} with the inward diffusion of oxygen along the catalyst surface.

3.3. Electrocatalysis of FAO

The FAO on a pure Pt surface is well-known to proceed *via* a dual-pathway mechanism. The produced intermediate CO molecules from the dehydration reaction can poison the Pt

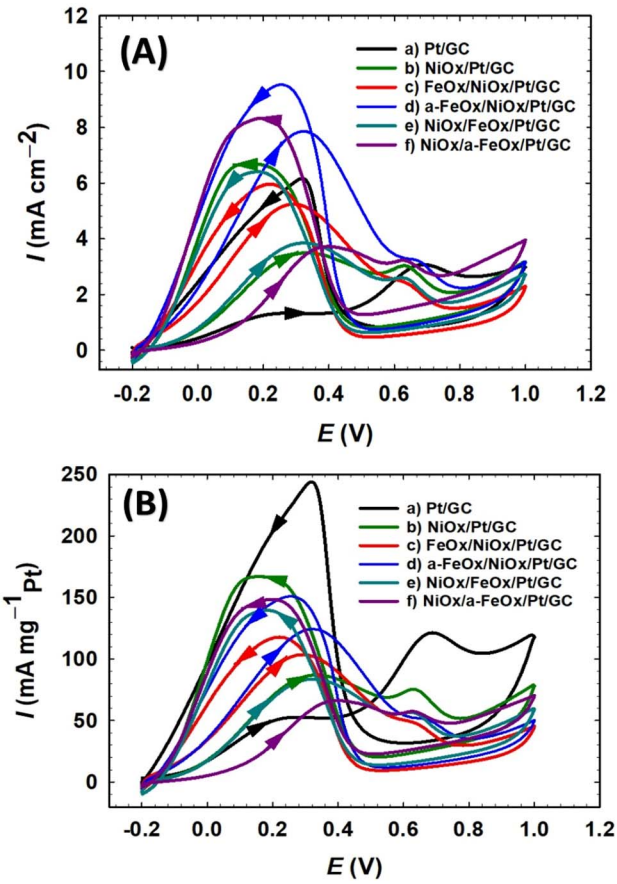

Fig. 5 CV curves of specific (A) and mass (B) activities for the FAO on the Pt/GC (a), NiO_x/Pt/GC (b), FeO_x/NiO_x/Pt/GC (c), a-FeO_x/NiO_x/Pt/GC (d), NiO_x/FeO_x/Pt/GC (e), and NiO_x/a-FeO_x/Pt/GC (f) catalysts obtained in 0.3 mol L^{-1} FA (pH = 3.5) aqueous solution.

Table 2 A summary of the important catalytic indices of Fig. 5B

Electrode	I_p^d (mA mg_{Pt}^{-1})	I_p^{ind} (mA mg_{Pt}^{-1})	I_b (mA mg_{Pt}^{-1})	I_p^d/I_p^{ind}	I_p^d/I_b
Pt/GC	42.7	21.4	237.2	2.0	0.18
NiO_x/Pt/GC	85.0	10.3	151.0	8.3	0.56
FeO_x/NiO_x/Pt/GC	94.1	5.8	108.6	16.0	0.87
a-FeO_x/NiO_x/Pt/GC	125.0	5.0	143.7	25.0	0.87
NiO_x/FeO_x/Pt/GC	84.0	6.6	125.0	12.7	0.67
NiO_x/a-FeO_x/Pt/GC	65.0	7.2	127.0	9.0	0.51

surface and inhibit its catalytic activity. In the forward scan of the CV plots of the prepared catalysts, two types of peak currents (I_p^d and I_p^{ind}) were observed. The first peak current (I_p^d) at ~0.3 V and the second peak current (I_p^{ind}) at ~0.65 V were credited to the direct oxidation of FA to CO_2 (dehydrogenation process) and the oxidation of CO produced from FA (dehydration process), respectively.[1,46] As shown in Fig. 5, the electrocatalytic behavior of the various modified electrodes toward FAO is determined by measuring the CVs in 0.3 mol L^{-1} FA (pH = 3.5) solution. The current ratio of these two peaks (I_p^d/I_p^{ind}) reflected the preferential oxidation pathway of FA at a particular catalyst. Fig. 5A & B summarize the activities of the different prepared nanocatalysts, in which the a-FeO_x/NiO_x/Pt/GC electrode exhibited the highest catalytic activity (I_p^d/I_p^{ind} = 25.0) and tolerance (I_p^d/I_b = 0.87) against the formation of the poisoning CO species. This activity of the a-FeO_x/NiO_x/Pt/GC electrode was about 12.5, 3.0, 2.8, 2.0, and 1.6 times higher than those of the Pt/GC, NiO_x/Pt/GC, NiO_x/a-FeO_x/Pt/GC, NiO_x/FeO_x/Pt/GC, and FeO_x/NiO_x/Pt/GC catalysts, respectively. Moreover, it was also noticed that there was a favorable negative shift (*ca.* 218 mV) in the onset potential (E_{onset}) of FAO reaction at the a-FeO_x/NiO_x/Pt/GC electrode relative to that of the Pt/GC electrode (see Tables 1 and 2). A key issue in the fabrication of the catalyst is its proper design that ensures a continuous and efficient use of its components, especially precious elements. For instance, nano-FeO_x and nano-NiO_x-modified GC electrodes do not show any electrocatalytic activity toward FAO; however, their binary mixtures with Pt showed much improved catalytic activities, *vide supra*. We also investigated the influence of the deposition sequence of nano-NiO_x and nano-FeO_x nanostructures (Fig. 5) on the electrocatalytic performance toward FAO. Fig. 5A & B (plots c) show the CVs of FAO at the FeO_x/NiO_x/Pt/GC electrode, whereas (plots e) in the same figures show the catalytic performance of the NiO_x/FeO_x/Pt/GC electrode. Interestingly, the FeO_x/NiO_x/Pt/GC electrode promoted a stronger catalytic activity toward FAO compared to the NiO_x/FeO_x/Pt/GC electrode. In other words, the deposition sequence of both nano-FeO_x and nano-NiO_x influenced the I_p^d and I_p^{ind} values. Thus, the ratios of I_p^d/I_p^{ind} and I_p^d/I_b were higher at the FeO_x/NiO_x/Pt/GC electrode (I_p^d/I_p^{ind} = 16.0 and I_p^d/I_b = 0.87, plot c in Fig. 5A & B) than those (I_p^d/I_p^{ind} = 12.7, I_p^d/I_b = 0.67, plots e in Fig. 5A & B) obtained for its "mirror image" electrode, NiO_x/FeO_x/Pt/GC. This emphasized the necessity of nano-FeO_x as the final layer atop the nano-NiO_x layer on the Pt/GC electrode; this sequence might be beneficial for enhancing the adsorption of FA but not the CO species. Interestingly, moreover, the activation of nano-FeO_x in the a-FeO_x/NiO_x/Pt/GC electrode (plots d in Fig. 5A & B) resulted in a superb enhancement of I_p^d (7.5 mA cm^{-2}) with a concurrent depression of I_p^{ind} (0.3 mA cm^{-2}) and thus increases in the I_p^d/I_p^{ind} and I_p^d/I_b ratios of the a-FeO_x/NiO_x/Pt/GC electrode. It seemed that the activation of iron oxide at −0.5 V might lead to the formation of iron oxide in different oxidation states, and

Table 3 A comparison of the electrocatalytic activities for several catalysts toward FAO

Electrode	I_p^d (mA cm^{-2})	I_p^{ind} (mA cm^{-2})	I_p^d/I_p^{ind}	I_p^d/I_b	Ref.
Pt black	0.458	1.828	0.250	0.231	56
Pt/MEA-C	0.077	0.547	0.141	0.658	56
Pt/PDAN/GC	0.61	0.84	0.72	0.90	57
2Pt4Pd/PVA/GO	0.92	1.23	0.75	0.69	64
Pd/Pt/PDAN/GC	1.51	1.23	1.20	0.77	57
Pt/NGA	4.63	7.48	0.62	0.71	58
Pt/BGA	5.57	10.08	0.55	0.58	58
Pt/GA	6.78	11.46	0.59	0.74	58
Pt/C	0.43	1.50	0.29	0.20	59
PtPd (2 : 1)/C	1.73	2.0	0.87	0.51	59
PtBiPd/C	—	—	0.89	0.27	63
NiO_x/Pt/GC	3.3	0.4	3.33–8.3	0.40–0.56	Ref. 31, this work
Au/Pt/GC (thin film)	—	—	3.44	0.54	60
Si-TiO_x/Pt/TiO_x (700 °C)	—	—	10.0	0.67	61
Nano-$PtAu_2$/C	4.0	5.06	0.79	—	11
MnO_x/Pt (θ_{MnO_x} = 30%)	7.6	0.5	15.2	0.85	62
FeO_x/NiO_x/Pt/GC	4.8	0.3	16.0	0.87	This work
a-FeO_x/NiO_x/Pt/GC	7.5	0.3	25.0	0.87	This work

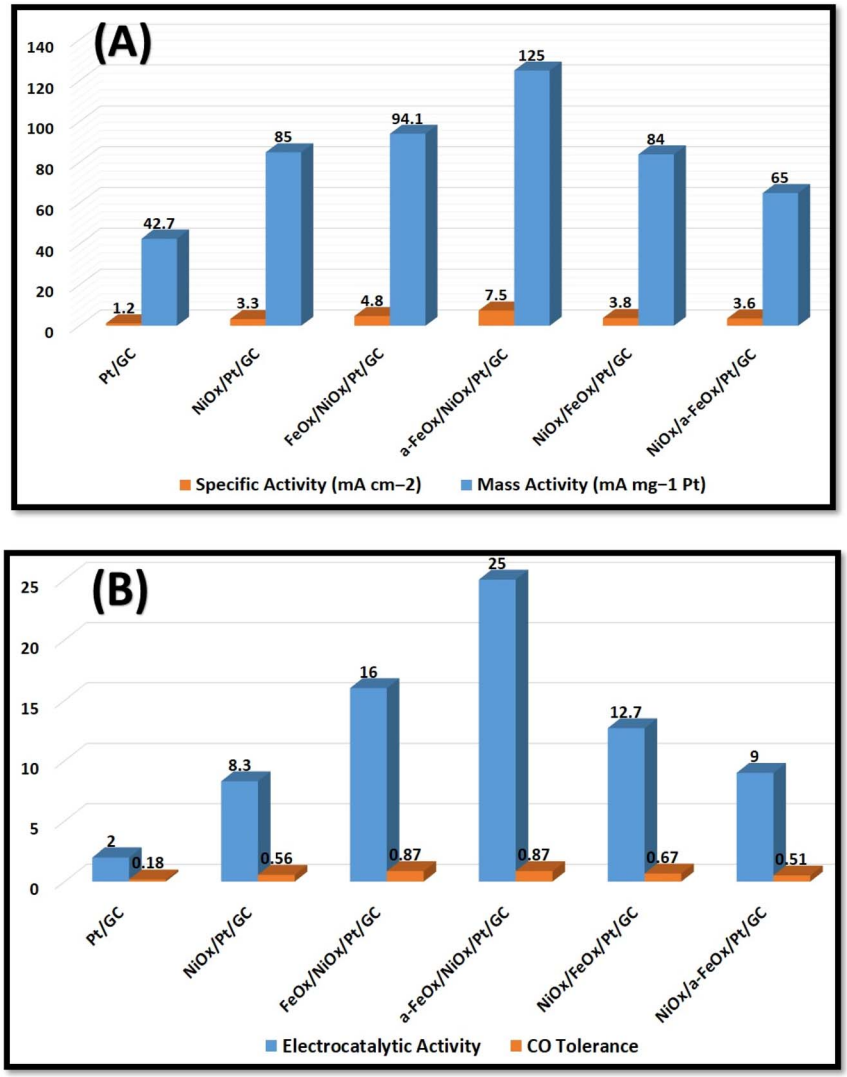

Fig. 6 Histograms of specific (I_p^d mA cm^{-2}) and mass activities (I_p^d mA mg$_{Pt}^{-1}$) (A), and electrocatalytic activity (I_p^d/I_p^{ind}) and CO tolerance (I_p^d/I_b) (B) of the Pt/GC, NiO_x/Pt/GC, FeO_x/NiO_x/Pt/GC, a-FeO_x/NiO_x/Pt/GC, NiO_x/FeO_x/Pt/GC, and NiO_x/a-FeO_x/Pt/GC electrocatalysts.

thus, the final nano-FeO_x surface structures retarded the formation of CO and/or accelerated its oxidative removal. Such findings indicated the great improvement of the ternary composition of FeO_x-NiO_x-Pt over the binary composition (NiO_x-Pt or FeO_x-Pt) in boosting FAO reaction in a synergism involving the three catalytic ingredients. From another projection, if the activity of the FeO_x/NiO_x/Pt/GC electrode is inspected relative to that of the FeO_x/Pt/GC electrode, one can easily notice the decrease, but in different proportions, of its I_p^d (3 times) and I_p^{ind} (10 times). Interestingly, the great reduction in the I_p^{ind} eventually enhanced the I_p^d/I_p^{ind} ratio from 5 for the FeO_x/Pt/GC electrode[6] to 16 for the FeO_x/NiO_x/Pt/GC electrode, an increase by a factor of *ca.* 3.2. In addition, the I_p^d/I_b ratio increased from 0.35 for the FeO_x/Pt/GC electrode to 0.87 in the case of the FeO_x/NiO_x/Pt/GC electrode (an increase by a factor of *ca.* 2.5), indicating an improved catalytic tolerance of the FeO_x/NiO_x/Pt/GC electrode against CO poisoning. In Fig. 5A, specific activities were normalized to the real surface areas that were

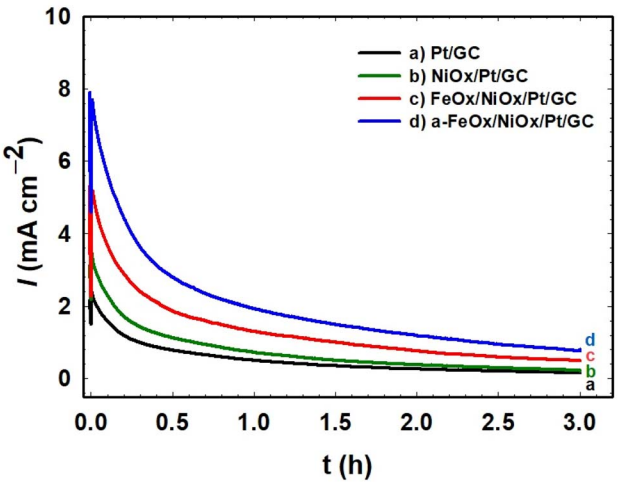

Fig. 7 Current–time relation obtained during the potentiostatic oxidation of formic acid at 0.3 V on the Pt/GC (a), NiO_x/Pt/GC (b), FeO_x/NiO_x/Pt/GC (c), and a-FeO_x/NiO_x/Pt/GC (d) electrodes in 0.3 mol L^{-1} HCOOH (pH = 3.5).

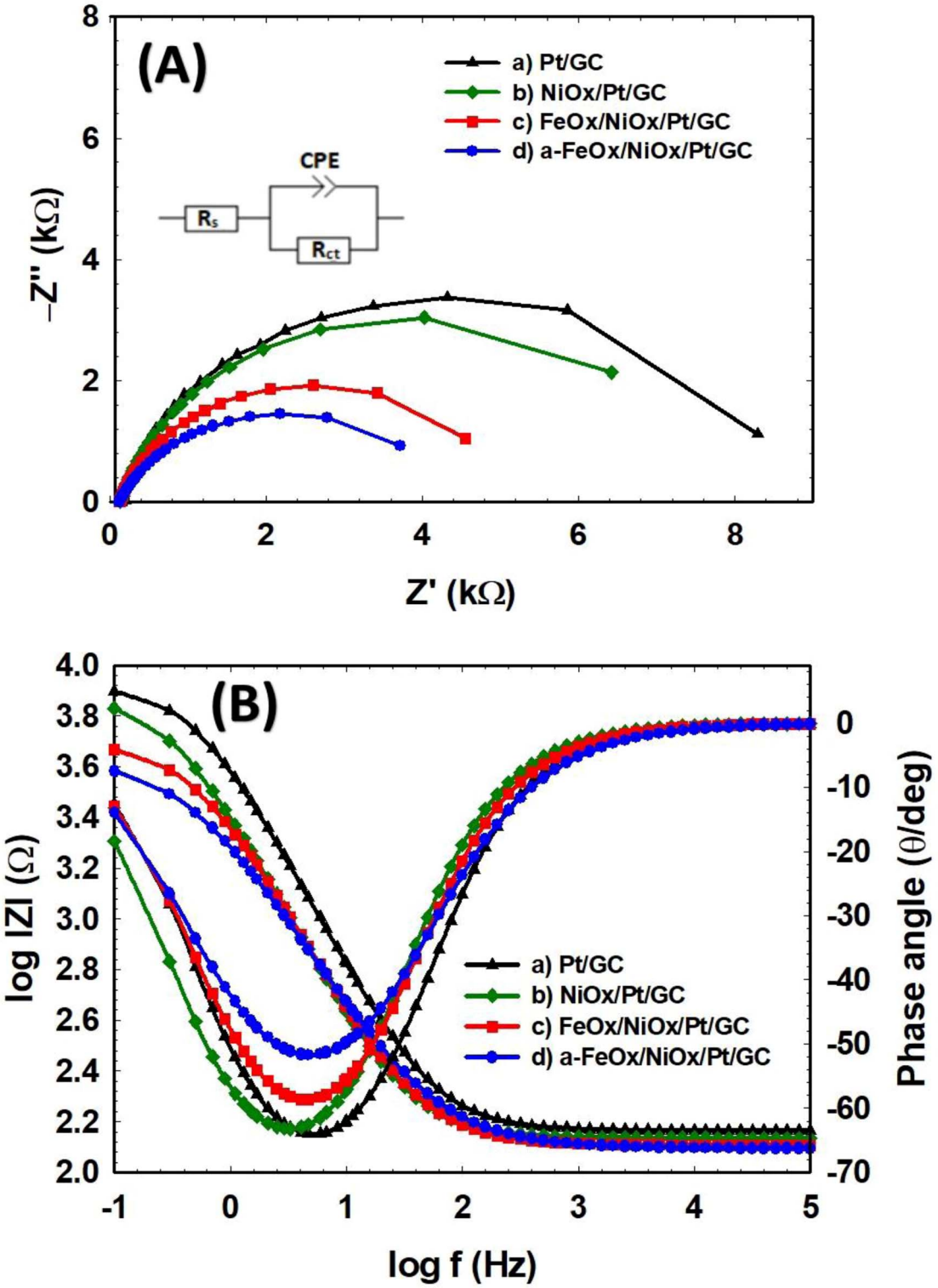

Fig. 8 Nyquist (A) and Bode (B) plots of the Pt/GC (a), NiO_x/Pt/GC (b), FeO_x/NiO_x/Pt/GC (c), and a-FeO_x/NiO_x/Pt/GC (d) electrodes obtained at 0.1 V in 0.3 mol L^{-1} FA (pH 3.5) and equivalent circuit of the system (inset in (A)).

calculated from Fig. 2.[31,54] On the other hand, in Fig. 5B, mass activities were normalized to the mass of Pt that was computed from the charge (Q) related to the i–t curve obtained during deposition according to Faraday's law (Fig. S3†).[55] Interestingly, this ternary FeO_x/NiO_x/Pt/GC catalyst was superior to several other catalysts toward FAO, according to the literature (see Table 3).[11,31,56–64]

Fig. 6A & B summarize the activities of these investigated electrocatalysts toward FAO, in which the a-FeO_x/NiO_x/Pt/GC exhibited the highest catalytic activities (I_p^d = 7.5 mA cm^{-2} =

125.0 mA mg_{Pt}^{-1}). This denoted *ca.* 6.3, 2.3, 2.1, 2.0, and 1.6 times higher specific activity than that observed for the Pt/GC, NiO_x/Pt/GC, NiO_x/a-FeO_x/Pt/GC, NiO_x/FeO_x/Pt/GC, and FeO_x/NiO_x/Pt/GC catalysts, respectively.

3.4. Stability of the catalysts

Chronoamperometry (CA) measurements were performed to check the stability of the investigated catalysts. The CA of the Pt/GC, NiO_x/Pt/GC, FeO_x/NiO_x/Pt/GC, and a-FeO_x/NiO_x/Pt/GC electrodes were conducted in 0.3 mol L^{-1} FA (pH = 3.5) at 0.3 V for 3 h. As shown in Fig. 7, the current density profile of the a-FeO_x/NiO_x/Pt/GC catalyst is much higher than that of the other investigated catalysts. For instance, after a period of 3 h, the current densities were *ca.* 1.0, 0.6, 0.2, and 0.2 mA cm^{-2} for the a-FeO_x/NiO_x/Pt/GC, FeO_x/NiO_x/Pt/GC, NiO_x/Pt/GC, and Pt/GC electrodes, respectively. Thus, it is clearly seen that the a-FeO_x/NiO_x/Pt/GC catalyst maintained the maximum current density among these catalysts, indicating a high stability of the catalyst toward FAO and unlikely electrochemical oxidative dissolution pathways. It should be noted here that the initial decay in the current density from these electrodes might be caused by a different degree of accumulation by CO_{ads} at the electrode's surface.[22,65] Also, a partial dissolution and/or detachment of nano-NiO_x and/or nano-FeO_x might be possible. Moreover, the observed decay in current density might originate as a transition from the catalytically active to the less active/inactive phases of nano-NiO_x and/or nano-FeO_x.[26]

3.5. Impedance measurements

To further elaborate on the electron transfer kinetics of FAO on the as-prepared Pt/GC, NiO_x/Pt/GC, FeO_x/NiO_x/Pt/GC, and a-FeO_x/NiO_x/Pt/GC electrodes, selected EIS measurements were then performed. Fig. 8 shows the representative Nyquist impedance (Fig. 8A) and Bode plots (Fig. 8B) recorded in 0.3 mol L^{-1} FA (pH 3.5) at 0.1 V in the frequency range of 10 mHz to 100 kHz. The EIS spectra were fitted to the chosen equivalent circuit (inset of Fig. 8A) using the EC-Lab software. Table 4 compares the EIS parameters (R_s: solution resistance, R_{ct}: charge transfer resistance, and CPE: constant phase element) for the different catalyst/electrolyte systems of this investigation. The Nyquist plots are mostly composed of semicircles where the diameter of each semicircle was proportioned to R_{ct} of the same catalyst in a correlation to its catalytic activity. A smaller semicircle diameter implies a faster reaction kinetics, which results in a higher catalytic activity.[66] As seen in Fig. 8A, R_{ct} increases in the order a-FeO_x/NiO_x/Pt/GC < FeO_x/NiO_x/Pt/GC < NiO_x/Pt/GC < Pt/GC. The R_{ct} of the FeO_x/NiO_x/Pt/GC and a-FeO_x/NiO_x/Pt/GC catalysts were obviously smaller than those of the NiO_x/Pt/GC and Pt/GC electrodes, indicating a faster FAO on the surfaces of the ternary FeO_x/NiO_x/Pt/GC and a-FeO_x/NiO_x/Pt/GC catalysts. Thus, the existence of nano-FeO_x, especially after activation, alleviated the CO poisoning on the Pt surfaces. The a-FeO_x/NiO_x/Pt/GC catalyst displayed the smallest semicircle (R_{ct} = 4.27 kΩ), revealing the fastest rate of FAO on its surfaces. Thus, through the above experimental comparisons, it was found that a-FeO_x/NiO_x/Pt/GC catalyst demonstrated the best electrocatalytic activity toward FAO among all the catalysts prepared in this investigation.

Table 4 Impedance parameters obtained during FAO at the Pt/GC, NiO_x/Pt/GC, FeO_x/NiO_x/Pt/GC, and a-FeO_x/NiO_x/Pt/GC electrodes. The data were obtained from the corresponding EIS spectra (Fig. 8)

Electrode	R_s [kΩ]	R_{ct} [kΩ]	CPE [$\mu Fs^{(\alpha-1)}$]	α
Pt/GC	0.145	8.40	43.66	0.8697
NiO_x/Pt/GC	0.136	7.57	74.00	0.8623
FeO_x/NiO_x/Pt/GC	0.127	4.98	77.43	0.8374
a-FeO_x/NiO_x/Pt/GC	0.124	4.27	102.50	0.7607

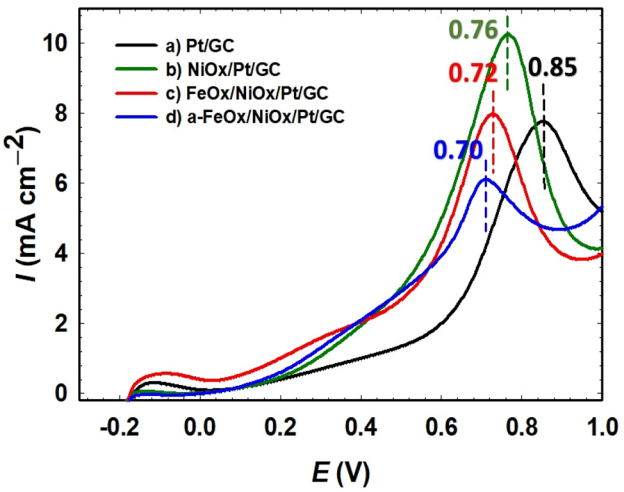

Fig. 9 CO stripping voltammograms of Pt/GC (a), NiO_x/Pt/GC (b), FeO_x/NiO_x/Pt/GC (c), and a-FeO_x/NiO_x/Pt/GC (d) electrodes in 0.5 mol L^{-1} H_2SO_4 solution.

3.6. Electrochemical performance analysis

The oxidation of CO was examined to quantitatively estimate its amount on the different inspected catalysts. The improvement of the FAO on Pt by the addition of metal oxide(s) might be caused by the preferred reaction in the dehydrogenation (third-body and/or electronic effect) or by the efficient removal of CO_{ads} produced in the dehydration route (bifunctional effect).[30] The CO-stripping measurements were carried out by holding the catalysts in 0.5 mol L^{-1} FA solution for 10 min to saturate the electrolyte as well as allow for the adsorption of CO on the electrocatalysts' surfaces. The adsorbed CO species were then desorbed electrochemically during the CV scan shown in Fig. 9. The primary CO oxidation peaks on the Pt/GC, NiO_x/Pt/GC, FeO_x/NiO_x/Pt/GC, and a-FeO_x/NiO_x/Pt/GC electrodes were located at 0.85, 0.76, 0.72, and 0.70 V, respectively, which indicated a stronger CO adsorption on the "pristine" Pt surface compared to the Pt-modified electrodes. The oxidation peaks potential for CO oxidation on the NiO_x/Pt/GC, FeO_x/NiO_x/Pt/GC, and a-FeO_x/NiO_x/Pt/GC electrodes, however, were negatively shifted, indicating weaker CO adsorption bonds on the Pt active sites in the presence of the deposited metal oxides (nano-NiO_x and/or nano-FeO_x). The presence of nano-NiO_x and nano-FeO_x

structures on the surface of the Pt/GC electrode was expected to increase the amount of oxygen and oxygen-containing functional groups and thus minimized the adsorption of CO_{ads} and the associated poisoning effects.

4. Conclusion

The current work demonstrated that the deposition of ferric oxyhydroxide nanoparticles on the surface of NiO_x/Pt/GC was critical in improving the catalytic activity (especially with activation at −0.5 V in 0.2 mol L^{-1} NaOH) for the FAO. The prepared a-FeO_x/NiO_x/Pt/GC electrode exhibited a catalytic enhancement that is ∼12.5-folds higher, with 214 mV negative shift in the E_{onset} for FAO and a 5-fold better durability compared to the Pt/GC electrode. The modification of the Pt/GC electrode with nano-NiO_x and nano-FeO_x nanoparticles provided the presence of surface functionalities and structures that synergistically improved FAO, possibly by favoring the direct route (dehydrogenation) on the expense of the unfavorable indirect route (dehydration). Interestingly, the a-FeO_x/NiO_x/Pt/GC catalyst exhibited a significant increase in the I_p^d (from 1.2 mA cm^{-2}, as observed for the Pt/GC electrode, to 7.5 mA cm^{-2}) and decrease in the I_p^{ind} (from 0.6 mA cm^{-2}, as observed for the Pt/GC electrode, to 0.3 mA cm^{-2}). In addition, the EIS and CO stripping inspections proved the enhanced charge transfer kinetics in the case of the FeO_x/NiO_x/Pt/GC electrode compared to the other investigated electrodes. Thus, the FeO_x/NiO_x/Pt/GC surface is considered as a good candidate for the electrochemical FAO.

Conflicts of interest

There are no conflicts to declare.

Acknowledgements

This work was supported by the Faculty of Science at Cairo University.

References

1 Y. Sun, B. Huang, Y. Li, Y. Qin, Z. Fu, M. Sun, L. Wang and S. Guo, *Fundam. Res.*, 2021, **1**, 453–460.
2 W. Luo, Y. Jiang, M. Wang, D. Lu, X. Sun and H. Zhang, *RSC Adv.*, 2023, **13**, 4803–4822.
3 L. Yang, Y. Wang, H. Feng, H. Zeng, C. Tan, J. Yao, J. Zhang, L. Jiang and Y. Sun, *Chem.–Asian J.*, 2021, **16**, 34–38.
4 S. Ha, R. Larsen, Y. Zhu and R. Masel, *Fuel Cells*, 2004, **4**, 337–343.
5 X. Hu, J. Zou, H. Gao and X. Kang, *J. Colloid Interface Sci.*, 2020, **570**, 72–79.
6 B. A. Al-Qodami, H. H. Alalawy, I. M. Al-Akraa, S. Y. Sayed, N. K. Allam and A. M. Mohammad, *Int. J. Hydrogen Energy*, 2022, **47**, 264–275.
7 I. M. Al-Akraa, B. A. Al-Qodami, M. S. Santosh, R. Viswanatha, A. K. Thottoli and A. M. Mohammad, *Int. J. Electrochem. Sci.*, 2020, **15**, 5597–5608.
8 M. Liang, T. Xia, H. Gao, K. Zhao, T. Cao, M. Deng, X. Ren, S. Li, H. Guo and R. Wang, *Nano Res.*, 2022, **15**, 1221–1229.
9 S. Luo, W. Chen, Y. Cheng, X. Song, Q. Wu, L. Li, X. Wu, T. Wu, M. Li and Q. Yang, *Adv. Mater.*, 2019, **31**, 1903683.
10 A. M. Mohammad, I. M. Al-Akraa and M. S. El-Deab, *Int. J. Hydrogen Energy*, 2018, **43**, 139–149.
11 X. Wen, S. Yin, H. Yin and Y. Ding, *Electrochim. Acta*, 2021, **373**, 137884.
12 Y. Zhu, Y. Pan, Y. Zhu, H. Jiang, J. Shen and C. Li, *J. Colloid Interface Sci.*, 2021, **593**, 244–250.
13 Y.-X. Wang, C.-F. Liu, M.-L. Yang, X.-H. Zhao, Z.-X. Xue and Y.-Z. Xia, *Chin. Chem. Lett.*, 2017, **28**, 60–64.
14 J. V. Perales-Rondón, S. Brimaud, J. Solla-Gullón, E. Herrero, R. J. Behm and J. M. Feliu, *Electrochim. Acta*, 2015, **180**, 479–485.
15 D. M. Sayed, G. A. El-Nagar, S. Y. Sayed, B. E. El-Anadouli and M. S. El-Deab, *Electrochim. Acta*, 2018, **276**, 176–183.
16 V. Briega-Martos, J. Solla-Gullón, M. T. Koper, E. Herrero and J. M. Feliu, *Electrochim. Acta*, 2019, **295**, 835–845.
17 Y. Chen, H.-J. Niu, Y.-G. Feng, J.-H. Wu, A.-J. Wang, H. Huang and J.-J. Feng, *Appl. Surf. Sci.*, 2020, **510**, 145480.
18 G. A. El-Nagar, A. M. Mohammad, M. S. El-Deab and B. E. El-Anadouli, *ACS Appl. Mater. Interfaces*, 2017, **9**, 19766–19772.
19 D. Minudri, A. Tesio, F. Fungo, R. Palacios, P. Cappellari, E. Pastor, G. Planes and A. Palpalá, *J. Power Sources*, 2021, **483**, 229189.
20 Y. M. Asal, A. M. Mohammad, S. S. Abd El Rehim and I. M. Al-Akraa, *J. Saudi Chem. Soc.*, 2022, 101437.
21 S. Chen and A. Chen, in *Encycl. Inter. Chem.*, ed. K. Wandelt, Elsevier, Oxford, 2018, pp. 607–619, DOI: 10.1016/B978-0-12-409547-2.13321-9.
22 G. A. El-Nagar and A. M. Mohammad, *Int. J. Hydrogen Energy*, 2014, **39**, 11955–11962.
23 H. H. Farrag, I. M. Al-Akraa, N. K. Allam and A. M. Mohammad, *Arabian J. Chem.*, 2023, **16**, 104524.
24 M. Lv, W. Li, H. Liu, W. Wen, G. Dong, J. Liu and K. Peng, *Chin. J. Catal.*, 2017, **38**, 939–947.
25 S. Chen, Q. Yuan and X. Wang, *Chem. Commun.*, 2023, **59**, 2473–2476.
26 G. A. El-Nagar, A. M. Mohammad, M. S. El-Deab and B. E. El-Anadouli, *J. Electrochem. Soc.*, 2012, **159**, F249.
27 Z.-F. Wu, Z.-Q. Jiang, Y.-K. Jin, F. Xiong, G.-H. Sun and W.-X. Huang, *Chin. J. Catal.*, 2016, **37**, 1738–1746.
28 Y. Xie and N. Dimitrov, *Appl. Catal., B*, 2020, **263**, 118366.
29 H. Shi, F. Liao, W. Zhu, C. Shao and M. Shao, *Int. J. Hydrogen Energy*, 2020, **45**, 16071–16079.
30 G. A. El-Nagar, A. M. Mohammad, M. S. El-Deab and B. E. El-Anadouli, *Electrochim. Acta*, 2013, **94**, 62–71.
31 I. M. Al-Akraa, A. E. Salama, Y. M. Asal and A. M. Mohammad, *Arabian J. Chem.*, 2021, **14**, 103383.
32 B. A. Al-Qodami, H. H. Farrag, S. Y. Sayed, N. K. Allam, B. E. El-Anadouli and A. M. Mohammad, *J. Nanotechnol.*, 2018, **2018**, 4657040.
33 B. A. Al-Qodami, H. H. Alalawy, S. Y. Sayed, I. M. Al-Akraa, N. K. Allam and A. M. Mohammad, *RSC Adv.*, 2022, **12**, 20395–20402.

34 Y.-X. Chen, S.-P. Chen, Q.-S. Chen, Z.-Y. Zhou and S.-G. Sun, *Electrochim. Acta*, 2008, **53**, 6938–6943.
35 Z. Dongsheng, G. Wenqiang, C. Guozhang, L. Shuai, J. Weizhou and L. Youzhi, *Adv. Powder Technol.*, 2019, **30**, 581–589.
36 S. Banik, A. Mahajan, S. R. Chowdhury and S. K. Bhattacharya, *RSC Adv.*, 2016, **6**, 92490–92501.
37 M. Saleh, *Curr. Top. Electrochem.*, 2014, **18**, 45–70.
38 C. X. Guo and C. M. Li, *Nano Energy*, 2017, **42**, 166–172.
39 M. Nagasaka, H. Yuzawa, T. Horigome, A. P. Hitchcock and N. Kosugi, *J. Phys. Chem. C*, 2013, **117**, 16343–16348.
40 M. Ding, T. Liu, Y. Zhang, Z. Cai, Y. Yang and Y. Yuan, *R. Soc. Open Sci.*, 2019, **6**, 181309.
41 M. S. El-Deab and T. Ohsaka, *J. Electrochem. Soc.*, 2007, **155**, D14.
42 M. G. Abd El-Moghny, H. H. Alalawy, A. M. Mohammad, A. A. Mazhar, M. S. El-Deab and B. E. El-Anadouli, *Int. J. Hydrogen Energy*, 2017, **42**, 11166–11176.
43 G. Cabello, R. A. Davoglio, F. W. Hartl, J. F. Marco, E. C. Pereira, S. R. Biaggio, H. Varela and A. Cuesta, *Electrochim. Acta*, 2017, **224**, 56–63.
44 C. Prabhu, A. Valechha, S. Wanjari, N. Labhsetwar, S. Kotwal, T. Satyanarayanan and S. Rayalu, *J. Mol. Catal. B: Enzym.*, 2011, **71**, 71–78.
45 A. C. Garcia, E. B. Ferreira, V. V. S. de Barros, J. J. Linares and G. Tremiliosi-Filho, *J. Electroanal. Chem.*, 2017, **793**, 188–196.
46 A. O. Elnabawy, J. A. Herron, J. Scaranto and M. Mavrikakis, *J. Electrochem. Soc.*, 2018, **165**, J3109.
47 I. M. Sadiek, A. M. Mohammad, M. E. El-Shakre and M. S. El-Deab, *Int. J. Hydrogen Energy*, 2012, **37**, 68–77.
48 Y. Jia, T. Luo, X.-Y. Yu, Z. Jin, B. Sun, J.-H. Liu and X.-J. Huang, *New J. Chem.*, 2013, **37**, 2551–2556.
49 D. Kumar, H. Singh, S. Jouen, B. Hannoyer and S. Banerjee, *RSC Adv.*, 2015, **5**, 7138–7150.
50 R. Chen, S. Zhao, H. Liu, X. Song and Y. Wei, *J. Photochem. Photobiol., A*, 2015, **312**, 73–80.
51 S. Wu, J. Lu, Z. Ding, N. Li, F. Fu and B. Tang, *RSC Adv.*, 2016, **6**, 82118–82130.
52 H. Zhang, J. Wang, X. Zhang, B. Li and X. Cheng, *Chem. Eng. J.*, 2019, **369**, 834–844.
53 J. Parhizkar and M. H. Habibi, *J. Water Environ. Nanotechnol.*, 2019, **4**, 17–30.
54 A. L. Ong, K. K. Inglis, D. K. Whelligan, S. Murphy and J. R. Varcoe, *Phys. Chem. Chem. Phys.*, 2015, **17**, 12135–12145.
55 J. Hu, S. Xue, O. Schneider, G. Yesilbas, A. Knoll and X. Huang, *Electrochem. Commun.*, 2020, **119**, 106826.
56 M. J. Ooi and A. A. Aziz, *Int. J. Hydrogen Energy*, 2017, **42**, 9063–9068.
57 A. Shatla, K. Hassan, A. Abd-El-Latif, A. Hathoot, H. Baltruschat and M. Abdel-Azzem, *J. Electroanal. Chem.*, 2019, **833**, 231–241.
58 M. S. Çögenli and A. B. Yurtcan, *Int. J. Hydrogen Energy*, 2020, **45**, 650–666.
59 M. S. Çögenli and A. B. Yurtcan, *Int. J. Hydrogen Energy*, 2018, **43**, 10698–10709.
60 I. M. Al-Akraa, Y. M. Asal and A. M. Mohammad, *J. Nanomater.*, 2019, **2019**, 2784708.
61 I. M. Al-Akraa and A. M. Mohammad, *Arabian J. Chem.*, 2020, **13**, 4703–4711.
62 M. S. El-Deab, *J. Adv. Res.*, 2010, **1**, 87–93.
63 L. Sui, W. An, C. K. Rhee and S. H. Hur, *J. Electrochem. Sci. Technol.*, 2020, **11**, 84–91.
64 S. Saipanya, L. Fang, S. Themsirimongkon, S. Maturost, N. Pongpichayakul, N. Promsawan and P. Waenkaew, *Polym. Adv. Technol.*, 2023, **34**, 120–133.
65 W. Chen and S. Chen, *J. Mater. Chem.*, 2011, **21**, 9169–9178.
66 W.-L. Qu, Z.-B. Wang, Y. Gao, C. Deng, R.-H. Wang, L. Zhao and X.-L. Sui, *Int. J. Hydrogen Energy*, 2018, **43**, 407–416.